

Synthesis and Characterization of the Magnesium/Boron Solid Solutions for Energetic Applications

Prawal P. K. Agarwal¹, Devon Jensen², Chien-Hua Chen², Robert M. Rioux^{1,3}, Themis Matsoukas^{1*}

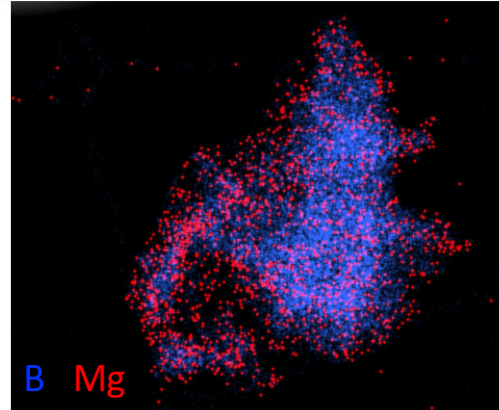
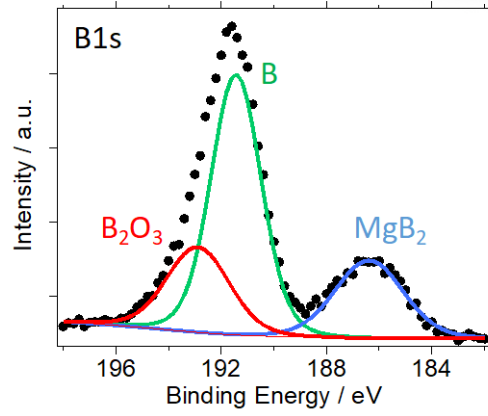
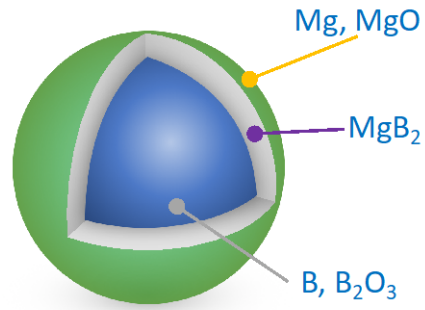
¹Department of Chemical Engineering, The Pennsylvania State University, University Park, Pennsylvania 16802, United States

²Advanced Cooling Technologies, Inc., Lancaster, Pennsylvania 17601, United States

³Department of Chemistry, The Pennsylvania State University, University Park, Pennsylvania 16802, United States

*E-mail of Corresponding Author: txm11@psu.edu

Table of Contents Graphic



ABSTRACT

A major problem limiting boron (B) use as a fuel or fuel additive is the native oxide layer present at the surface, which acts as a diffusion barrier at the boron/oxidizer interface. A requirement for improving the reactivity and exothermicity during the oxidation of B particles is to reduce the thickness of the native oxide. This can be achieved by the addition of reactive metals with reasonable gravimetric energy density, such as Mg, in the form of a mechanical mixture or alloyed compounds, which can undergo an exothermic redox reaction to reduce native oxide and enrich metallic B. Herein, we develop an approach to synthesize Mg/B solid solutions through a self-propagating high-temperature synthesis (SHS) reaction at 500°C leading to the formation of an outer shell comprised of Mg, MgO, and MgB₂ around a B core as demonstrated by X-ray photoelectron spectroscopy (XPS), X-ray diffraction (XRD), and high-angle annular dark-field - scanning transmission electron microscopy - energy dispersive spectroscopy (HAADF-STEM-EDS). Particle size analysis by dynamic light scattering (DLS) shows a size distribution with an average size of 550 nm. The low synthesis temperature minimizes sintering and is inherently free of organic contamination compared to other available methods. The core-shell architecture offers two advantages: extension of the shelf life of B particles by the formation of a passivation shell; and in addition to the exothermic oxidation of Mg, MgB₂, and B, an exothermic redox reaction occurs between Mg and native B₂O₃ to produce additional B fuel, culminating in a synergistic interaction that leads to increased heat release. Thermal analysis shows the promotional effect of Mg on B oxidation with increased heat release (24% higher) and higher oxidative stability than Mg and B under identical conditions. Synthesized Mg/B solid solutions release 90% of the theoretical energy density of Mg/B and thus show promise as energetic materials.

KEYWORDS: boron, magnesium, energetic materials, solid solutions, core-shell, thermal oxidation, heat release, combustion

1. INTRODUCTION

Metals and metalloids are highly energetic materials commonly added to rocket fuels and propellants to extract more energy and produce more thrust in volume-limited propulsion systems [1-6]. They possess higher gravimetric and volumetric energy density than hydrocarbon fuels, and as additives to liquid fuels, they offer the benefits of enhanced combustion efficiency and reduced exhaust emissions [3, 4]. Magnesium (Mg) and aluminum (Al), whose gravimetric energy densities are 25 kJ/g and 31 kJ/g, respectively, are among the most widely studied metals [1-4, 6]. Boron (B) ranks even higher. It is a prime candidate as a solid fuel and fuel additive with a gravimetric and volumetric energy density of 58 kJ/g and 140 kJ/mL [5-11]. A problem limiting the performance of B as an energetic material is the presence of a native oxide layer on its surface. While it provides temporary passivation during storage, the oxide layer acts as a diffusion barrier that hinders direct reaction between the oxidizer and metal, inhibits ignition kinetics, and leads to incomplete combustion [1-11]. Reducing the dimensions of B particles to the nano/submicron size leads to higher heat release and improved combustion kinetics [6-13]. The downside of B nanoparticles is the surface oxide layer that represents a more significant fraction of the mass and volume, which reduces their gravimetric and volumetric energy density [7-9]. Moreover, the tendency of small particles to aggregate into large assemblies is detrimental to the combustion performance of the fuel and causes issues associated with processing, including precipitation, deposition on pipe walls, and pump erosion during fuel transportation [3-6, 14, 15].

To overcome these limitations, four approaches are being studied in the literature: (a) use of organic coatings to passivate the surface of B particles [14, 16-18]; (b) *in-situ* reduction of the native oxide by hydrogen plasma followed by deposition of a passivating coating by plasma-enhanced chemical vapor deposition (PECVD) [19]; (c) use of borides to facilitate the transport of

the oxidizer through oxide layers [20, 21] and (d) use of catalytic dopants such as Al, Ni, and Mg to reduce the ignition delay and eliminate the B oxide through redox reactions [22-31]. Passivation of surfaces with organic compounds, such as alkoxy groups, organic acids, and polymers improves the shelf life of B particles, but the coating decreases the gravimetric energy density [16, 17]. Several studies [20-22] involving metal borides demonstrated high thermal stability and enhanced combustion kinetics. Due to increased thermal stability, metal borides such as AlB_2 and MgB_2 have a prolonged shelf life compared to their metallic counterparts [22-25]. Micron-sized metal borides have low reactivity, poor heat release, and require time-consuming, high-temperature processing [22-25]. Catalytic dopants such as Al, Mg, Fe, and Ni enhance the amount of heat released by reducing B oxide to elemental B during oxidation [22-31]. The ignition of the dopants raises the local temperature at the reaction interface, thereby enhancing the kinetics of B oxidation. These metals can be added as a mechanical mixture, or they can be coated on the surface of B particles to form a core-shell architecture with enhanced heat release. Mechanical mixtures have shorter shelf life due to the oxidative instability of the individual metal particles.

As a high-energy-density material, Mg has been successfully used as a propellant additive in aerospace and underwater propulsion systems [33-36]. It has good combustion characteristics and comparatively low melting ($\sim 600^\circ\text{C}$) and boiling ($\sim 1100^\circ\text{C}$) points, properties that facilitate ignition and promote complete oxidation [34, 35]. The addition of Mg as additives or in the form of a compound with B (MgB_2) further increases the extent of oxidation and improves combustion efficiency [35-40]. The preignition of Mg can induce the ignition of B by elevating the local temperature during oxidation [35-40]. The formation of ternary oxides containing Mg, B, and O delays the formation of B_2O_3 during oxidation and minimizes molten B_2O_3 impeding the oxidation of the underlying B metal. However, the measured heat release from Mg/B mechanical mixtures

and Mg borides was less than ~45% of the theoretical gravimetric energy density of B due to their incomplete oxidation and the presence of B oxide, which acts as a diffusional barrier during oxidation [35-40].

Guo et al. [21] synthesized MgB₂ powder by sintering and reported improved combustion performance over B particles (3 μm) in terms of heat release. They attributed the enhanced performance to the absence of a closed surface layer of B₂O₃ during the initial combustion stage due to the presence of Mg near the surface. The evaporation of Mg during thermal oxidation does not allow B₂O₃ to form a commensurate layer around the particles, allowing for more efficient combustion [23, 32-36]. Sun et al. [38] studied the effect of Mg incorporation on the combustion behavior of B by preparing sintered mixtures of B/MgB₂ from micron-sized B and Mg particles. Enhanced heat release was found for all Mg-containing samples compared to the B-only sample. The effect was more pronounced in Mg containing B due to the homogeneous distribution of Mg in the material achieved by annealing during the preparation step. Mg evaporated and evenly coated the surface of the B particles. Liang et al. [41] investigated the oxidation and decomposition during the combustion of MgB₂ particles using a laser combustion technique. Combustion time analysis showed the shortest ignition delay and longer combustion times of MgB₂ compared to B and Mg.

The desired Mg/B system should fulfill two objectives: (1) greater gravimetric heat release upon oxidation and (2) provide oxidative stability at low temperatures for improved handling and shelf life. We developed an approach for the dry synthesis of solid solutions by using a self-propagating high-temperature synthesis (SHS) reaction [30]. The SHS reaction is self-sustaining upon initiation. The molten metal interface quickly propagates towards the metal particles and diffuses into the surface oxide, converting the metal powder mixture into a solid solution [30]. If

both metals remain solid during the reaction, slow kinetics and low conversion are observed. If both metals melt during the reaction, the reaction occurs in the liquid phase through diffusion achieving complete conversion [30]. Here, we report the synthesis of energetic Mg/B solid solutions using the SHS reaction between B and Mg. Submicron-sized particles of B and Mg with high purity are used to synthesize core-shell structures of Mg/B via a dry process that uses no other chemicals beyond solid B and Mg, thereby ensuring high purity of the synthesized solid solutions. The thermochemical behavior of B particles is compared with Mg/B solid solutions to study the effects of the incorporation of Mg on their heat release and stability.

2. MATERIALS AND METHODS

Boron particles (99.5%; 500 nm; Nanoshel) and Mg particles (99.9%; 800 nm; US Research Nanomaterials) were used. The powders were mixed in a weight ratio of 1:1 into a glass vial using a three-step dry-mixing technique. This technique involves stirring with micro spatula, sonicating the dry mixture for 15 min at 25°C to break up aggregates, and magnetic agitation to form a homogeneous mixture. The mixture was then spread uniformly on the surface of a glass slide (1.1 mm thick, 25 × 75mm, Dot Scientific Inc.). After spreading the mixture, another glass slide was placed over the mixture and sides were then covered with Al foil. Pressing the mixture between glass slides reduces the exposure of particles to ambient air and promotes close contact between Mg and B, to facilitate effective atomic diffusion during heating [12, 13]. The glass slides were then placed in a muffle furnace (Model: FB1415M, Thermolyne) at 25°C and were heated at a heating rate of 30°C/min to 500°C. Isothermal conditions were maintained at 500°C for 90 min, after which the furnace was turned off and the sample was left inside to cool for 3 h. The schematic of the experimental procedure is illustrated in Figure 1. Working conditions (temperature) for the

synthesis were designed in accordance with the phase diagram of Mg-B system [40]. The process parameters such as synthesis temperature and time were optimized by performing thermal analysis experiments on various synthesized samples. Synthesized solid solutions were stored in vials prior to testing and characterization.



Figure 1. Schematic of the experimental method used for the synthesis of solid solutions of Mg/B.

X-ray diffraction (XRD) was performed on a Malvern Panalytical XPert Pro MPD theta-theta diffractometer using Cu K_{α} radiation to identify the phase of the dry sample. X-ray photoelectron spectroscopy (XPS) was employed to obtain detailed information about the chemical bonding of the near-surface region of the particles. XPS experiments were performed using a Physical Electronics VersaProbe II instrument equipped with a monochromatic Al K_{α} x-ray source ($h\nu = 1,486.7$ eV) and a concentric hemispherical analyzer. Charge neutralization was performed using low-energy electrons (< 5 eV) and positive argon ions. A fixed take-off angle of 45° to the sample surface plane was employed [42]. For analysis by scanning transmission electron microscopy (STEM) and energy dispersive spectroscopy (EDS), the particles were dispersed in ethanol (Purity: 95%; Anhydrous alcohol; IBI Scientific), and sonicated for 10 min by ultrasonication (Branson ultrasonicator (Model: CPX3800H)). Two drops of the dispersion were

deposited on a TEM lacey carbon copper grid (Electron Microscopy Sciences) using a micro dropper. STEM-EDS analysis was performed on a Talos F200X at 200 kV with an XFEG source with a minimum probe size of 0.16 nm and fitted with an integrated SuperX EDS detector. The imaging was performed in high-angle annular dark-field (HAADF). Thermogravimetric analysis (TGA) and differential scanning calorimetry (DSC) were performed on a TA Instruments Model Q600 SDT, which provides simultaneous measurement of heat flow (DSC) and weight change (TGA) on the sample from $\sim 20^{\circ}\text{C}$ to 1000°C . Analyses were conducted in ultra-zero air and ultra-high purity argon at a volumetric flow rate of 100 mL/min for all samples studied. The sample was placed in the alumina sample cups (90 μL , TA Instruments) and a heating rate of $20^{\circ}\text{C}/\text{min}$ was used. Particle size analysis was performed by dynamic light scattering (DLS) on a Malvern Zetasizer Nano ZS. Particles were added to ethanol at a concentration of 2.5 mg/L. The dispersion was sonicated for 10 min with Branson ultrasonicator (Model: CPX3800H). Three duplicate runs were performed on the sample at a temperature of 25°C .

3. RESULTS

The particle size distribution of the synthesized Mg/B solid solutions was determined by DLS. Figure 2 is the intensity-weighted particle size distribution of the particles dispersed in ethanol. The size distribution consists of a single peak in the range of 200-600 nm with a mean size of 550 nm. There is no peak in the 800 nm range, which corresponds to the mean size of the Mg particles. Clearly, Mg has reacted and is no longer present in its initial form.

Figure 3 is the XRD analyses of the synthesized Mg/B solid solutions (blue) and the mechanical mixture of Mg/B (purple), which is used as a control. The diffractograms demonstrate the presence of distinct phases after the synthesis of Mg/B solid solutions compared to the

mechanical mixture of Mg/B. The diffractograms of the Mg/B mechanical mixture contain peaks associated with Mg, MgO, B, and B₂O₃. Mg signals are prominent while the B signals are much weaker, which is attributed to the amorphous nature of the commercial B powder. MgO and B₂O₃ signals originate from the native oxides of Mg and B, respectively. The diffractogram of the synthesized Mg/B solid solutions is mainly composed of Mg, MgB₂, MgO, Mg₂B₂O₅, B, and B₂O₃ phases. However, less intense reflections due to B₂O₃ are observed in the solid solutions as compared to Mg/B mechanical mixtures. The phases formed during the SHS reaction (which were not present in Mg/B mechanical mixtures) are MgB₂ and Mg₂B₂O₅ (ternary oxide of Mg and B). Prominent reflections for Mg indicate its presence in the synthesized solid solutions. These results are consistent with the phase diagram of the Mg-B system, which demonstrates MgB₂ formation co-existing with unreacted Mg at ~500°C [40].

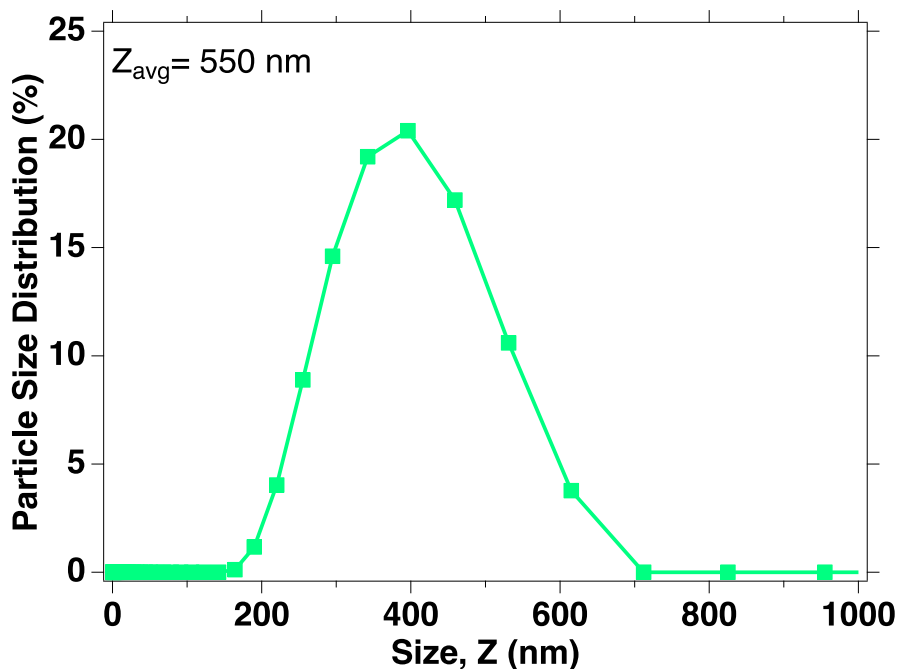


Figure 2. Intensity-weighted particle size distributions for a 2.5 mg/L dispersion of Mg/B solid solution particles in ethanol.

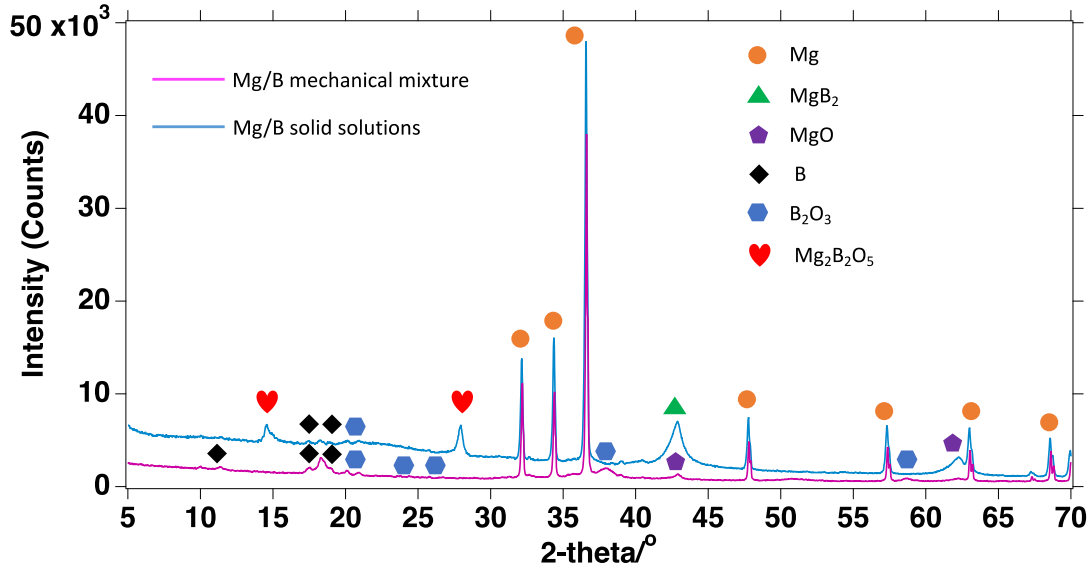


Figure 3. X-ray diffractograms comparing the presence of different phases of Mg and B in mechanical mixtures of Mg/B (purple) and Mg/B solid solutions (blue).

Figure 4a is an XPS survey scan revealing the presence of B, Mg, and oxygen (O) in the Mg/B solid solutions. Figure 4b is the fitted and deconvoluted high-resolution Mg 2s spectrum; the peak at ~88.5 eV corresponds to metallic Mg, while the major peak at ~90 eV corresponds to MgB₂. A peak at ~91.5 eV is due to the presence of MgO. The high-resolution O 1s spectrum in Figure 4c reveals two distinct peaks – a lower binding energy peak at ~532.5 eV corresponding to MgO and a higher energy peak at ~534.2 eV corresponding to B₂O₃. Figure 4d is a high-resolution B 1s spectrum. The major peak at the lower binding energy of ~187.6 eV indicates the presence of MgB₂. The other peaks in the B 1s spectrum at 190.3 eV and 193 eV correspond to metallic B and B₂O₃, respectively. The presence of B₂O₃ signals is attributed to the native oxide layer of B. XRD and XPS analysis demonstrate the Mg/B solid solutions consist mainly Mg, MgB₂, and B along with their oxides.

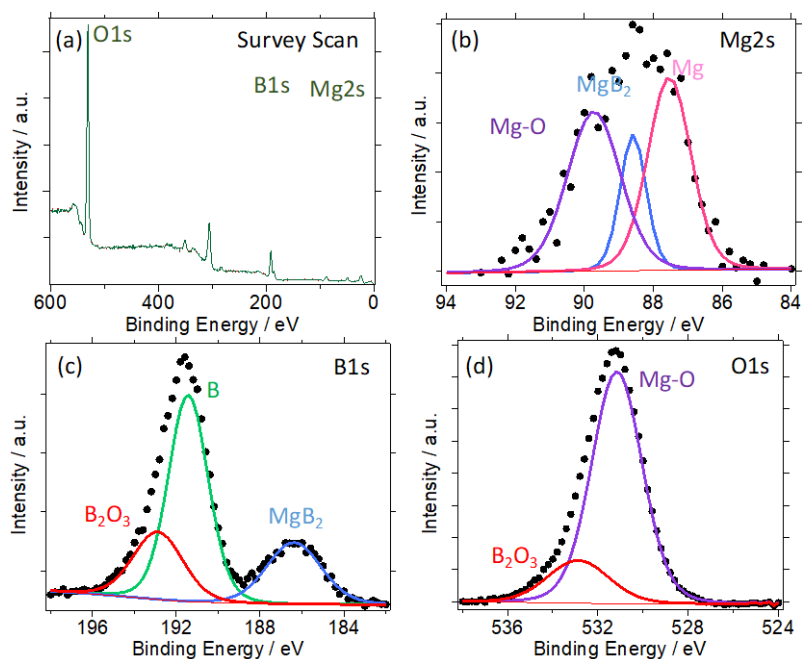


Figure 4. XPS analysis showing: (a) survey scan of Mg/B solid solutions; (b) high-resolution Mg 2s spectrum with Mg, MgB₂ and MgO chemical states; (c) high-resolution B 1s spectrum with MgB₂, B and B₂O₃ chemical states; and (d) high-resolution O 1s spectrum with MgO and B₂O₃ chemical states.

HAADF-STEM-EDS was used to generate elemental maps of Mg/B solid solutions. Figure 5a is a STEM image demonstrating the presence of both Mg and B in the synthesized particles. The darker phase corresponds to Mg (density: 1.7 g/cm³), which appears to be mainly in the near-surface regions with some present in the surface oxide, as shown in Figures 5a-b. It is not possible to differentiate between B and MgB₂ phases due to their similar material densities (B density: 2.4 g/cm³; MgB₂ density: 2.6 g/cm³). Mg is distinctly present on the surface of B particles (Figure 5a). Figure 5b combines elemental maps for B (blue) and Mg (red), revealing that Mg and MgB₂ are uniformly distributed over the B. This agrees with XPS analysis regarding the presence of Mg-rich

phases on the surface of the particle. Individual elemental maps of B and Mg provide additional evidence regarding the distribution of Mg at the surface and B in the core (Figure 5c-d).

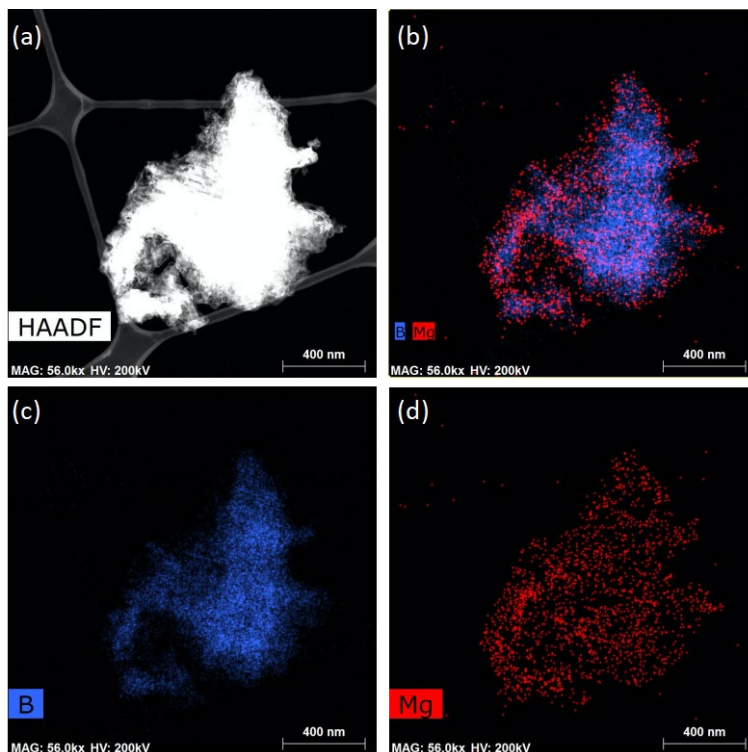


Figure 5. HAADF-STEM-EDS showing elemental maps: (a) STEM micrograph indicating the presence of Mg in the near-surface region of B; (b) combined elemental map of B and Mg demonstrating the distribution of Mg and B; (c) and (d) elemental micrographs of B and Mg, respectively.

The thermal oxidation behavior of the Mg/B solid solutions was studied (a) to analyze the oxidative stability of the system by comparison of its onset temperature to that of B; (b) to quantify and compare the extent of oxidation and experimental heat release before and after the incorporation of Mg into B particles, and (c) to test their extended shelf life of by measuring heat release after storage at ambient conditions for six months. The onset temperature, the temperature

at which ignition of the material begins, characterizes the oxidative stability of the material [38]. As observed in Figure 6, the onset temperature of Mg, B particles, and Mg/B solid solutions are 500°C, 550°C, and 625°C, respectively, indicating a delay of 75°C in the presence of Mg due to the formation of Mg-B and Mg-O bonds. Figure 6a shows TGA traces of Mg, B, and the synthesized Mg/B solid solutions in which the weight gain due to oxidation is shown as a function of temperature. Mg particles undergo oxidation and show a weight gain of 46% while B particles increase in weight by 146% upon thermal oxidation. Mg/B solid solutions containing a 1:1 weight ratio of B and Mg exhibit a weight gain of 106%, which is above the average weight gain of B and Mg. DSC analysis of Mg, B, and Mg/B solid solutions is shown in Figure 6b. Untreated Mg and B have their exothermic peaks between 500-750°C and 550-690°C, respectively, which amount to heat release of 14.5 kJ/g and 29 kJ/g. Mg/B solid solutions possess a small endothermic peak at 550°C due to the melting of Mg followed by a broad exothermic peak, which releases 36 kJ/g of heat in the temperature range of 540-850°C, 24% higher than B particles and 60% more than Mg particles. Compared to Mg and B, the Mg/B solution has a broader exothermic peak at ~850°C. By contrast, the mechanical mixture of Mg/B with the same bulk composition as the solid solution releases 26 kJ/g of heat, lower than both the pure B and the solid solution (Figure S1 in Supporting Information). Thermal analysis experiments were repeated in duplicate to ensure reproducibility of the results.

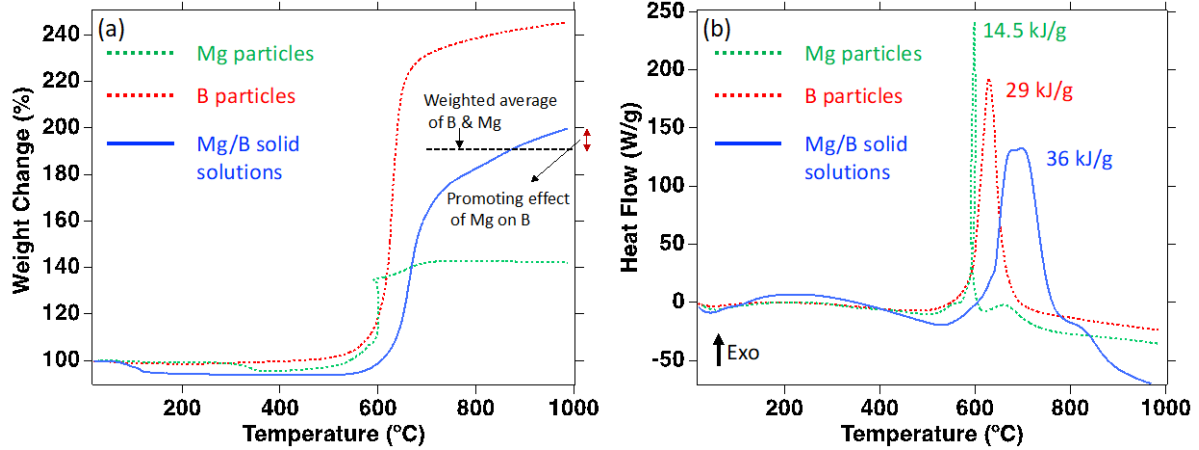


Figure 6. (a) TGA and (b) DSC analyses of Mg particles (green), B particles (red), and Mg/B solid solutions (blue) in air. The weight gain and heat release of all the samples are shown due to their thermal oxidation up to 1000°C.

Table 1 compares the theoretical oxidation enthalpy of B and Mg/B with the heat released during oxidation in the air up to 1000°C. B releases 50% of the theoretical heat during oxidation while the heat release for Mg/B is 90% of its theoretical energy density. This significant improvement in the percentage of heat release is observed after incorporation of Mg into the B system.

Table 1. Comparison of heat release of B particles and Mg/B solid solutions

Material	Theoretical Oxidation Enthalpy (kJ/g)	Experimental Heat Release (kJ/g)	Heat Extracted (%)
B particles	58	29	50
Mg/B solid solution	40	36	90

4. DISCUSSION

According to the phase and elemental analyses, MgB₂ and Mg₂B₂O₅ are present in addition to Mg, B, and B₂O₃. Potential chemical reactions during the synthesis of solid solutions are summarized in Table 2 along with Gibbs free energy at the synthesis temperature (500°C).

Table 2. Possible chemical reactions during the synthesis of Mg/B solid solutions.

Reaction number	Chemical Reaction	Gibbs Energy (ΔG) at 500°C (kJ/mol)
1	$\text{Mg (l)} + 2\text{B(s)} \rightarrow \text{MgB}_2\text{(s)}$	-86
2	$3\text{Mg(l)} + \text{B}_2\text{O}_3\text{(l)} \rightarrow 3\text{MgO(s)} + 2\text{B(s)}$	-488
3	$4\text{Mg(s)} + \text{B}_2\text{O}_3\text{(l)} \rightarrow \text{MgB}_2\text{(s)} + 3\text{MgO(s)}$	-569
4	$2\text{MgO(s)} + \text{B}_2\text{O}_3\text{(l)} \rightarrow \text{Mg}_2\text{B}_2\text{O}_5\text{(s)}$	-177

Mg can reduce B₂O₃ via reaction 2 to form B and MgO. The disappearance of the B₂O₃ peak from the diffractogram of Mg/B solid solutions suggests the reduction of B₂O₃ by Mg via reaction 2 and the occurrence of reaction 3 when excess Mg is present relative to B₂O₃. The large negative Gibbs free energies of reactions 2 and 3 indicate a strong driving force to form MgB₂ and MgO. The products of reaction 2 are MgO and B. The generation of B leads to the increase in the metallic B content in solid solutions. The formation of MgB₂ is most likely due to the reaction between Mg and B₂O₃, as suggested by thermodynamic analysis (Figure S2 in Supporting Information) and several studies in the literature [38, 40, 41]. By contrast, MgB₂ formation due to the direct reaction of Mg and B (reaction 1) is unlikely due to the small value of the Gibbs free energy. Both Mg and B₂O₃ react in the liquid state to form solid products MgB₂ and MgO. XPS confirmed their presence on the surface. The presence of MgB₂ and MgO on the surface can lead to surface passivation and hence an extended shelf life of synthesized Mg/B solutions. The diffractogram in Figure 3 contains reflections for Mg₂B₂O₅ that arise due to the reaction of solid MgO and liquid B₂O₃ (reaction 4) during SHS synthesis. The formation of that ternary oxide, Mg₂B₂O₅, entraps liquid B₂O₃ such

that its sintering effect is minimized [38, 39]. Hence, the net effect of these reactions is to enrich the solid solution in MgB_2 and B at the expense of less energetic Mg and of B_2O_3 , which does not significantly contribute to heat release during oxidation. A portion of unreacted Mg and B_2O_3 is apparently present as well as shown by XRD and XPS analyses (Figures 3 and 4). The presence of the metallic form is accompanied by oxides of Mg and B in the forms of MgO, $\text{Mg}_2\text{B}_2\text{O}_5$, and B_2O_3 . However, the percentage of heat extracted from Mg/B solutions during oxidation suggests these oxides are less than 10% as the heat release due to oxidation of metals present in solid solutions is 90% of the theoretical value of the Mg/B system as shown in Table 1. This suggests the synthesized Mg/B solutions are at least 90% pure. HAADF-STEM-EDS analyses (Figure 5) show the uniform distribution of Mg on the B surface, which confirms the formation of core-shell structures of Mg/B solutions leading to a few distinct advantages such as surface passivation and a large area of contact between various components leading to efficient thermal oxidation.

Hollow shells of MgO are also present (Figure S3 in Supporting Information) due to the Kirkendall effect, originating from an unequal diffusion couple between molten Mg and oxygen [43]. The presence of MgO is beneficial in using Mg/B solid solutions as secondary fuel additives in liquid propellants. Bello et al. [44] studied the combustion behavior of rocket propellants as a function of the concentration of MgO nanoparticles. Due to the addition of MgO, the evaporation rates of fuel droplets were improved by two orders of magnitude. A small endothermic peak corresponding to the melting of Mg at $\sim 540^\circ\text{C}$ is found in the DSC plot (Figure 6) prior to the exothermic oxidation peak, which is supported by the X-ray diffractograms and XPS spectra, exhibiting the presence of unreacted Mg in solid solutions (Figures 3 and 4). The presence of Mg near the surface helps elevate the localized temperature during thermal oxidation to intensify B oxidation.

As Mg/B solid solutions are synthesized from Mg and B in a weight ratio of 1:1, if Mg and B oxidize independently of each other, the anticipated specific weight gain should be the average of Mg and B, approximately 96%. However, the weight gain of Mg/B solid solutions due to oxidation is 106%, which is 10% higher than the average weight gain of Mg and B (Figure 6a). This confirms the promoting effect of Mg incorporation on B oxidation shown by a red arrow in Figure 6a, which is further corroborated by the DSC analysis (Figure 6b), which shows enhancement in heat release of B due to the presence of Mg. The higher onset temperature (625°C) of Mg/B solid solutions compared to Mg (500°C) and B particles (550°C) indicates improved oxidative stability of synthesized solid solutions due to the presence of MgO and MgB₂ on their surface [38, 45]. This suggests MgO and MgB₂ act as a passivation layer to the B core, thereby extending the shelf life of synthesized solid solutions. This was confirmed by thermal analysis of Mg/B solid solutions after six months of storage in ambient conditions (25°C, 60% RH (RH = relative humidity)) (Figure S4 in Supporting Information). The oxidative stability of solid solutions is due to the presence of Mg-B and Mg-O bonds on the surface, which lead to additional oxidative stability of the synthesized solid solutions unlike metals with highly reactive surfaces. This confirms our hypothesis that the presence of MgB₂ and MgO leads to passivation and extended shelf life. During thermal oxidation of the synthesized samples, the energy to break Mg-B bonds comes from the exothermic oxidation of Mg present on the surface [27, 28, 39]. To further understand whether there are other reactions occurring besides oxidation, DSC analysis of Mg/B solid solutions in an inert (Ar) atmosphere was performed (Figure 7). An exothermic peak with a heat release of ~4 kJ/g is observed with an onset temperature of 625°C, the same as the onset temperature for the exotherm observed in the air (Figure 6). This is due to the redox reaction between Mg and B₂O₃ within Mg/B solid solutions.

The overall heat release measured from a broad exotherm is due to the oxidation of Mg, MgB₂, B, and the redox reaction between B₂O₃ and Mg (Figure 7). Mg evaporates, which reacts with air to form MgO that is deposited as solid on the synthesized particles (reaction 5). B oxidizes to form B₂O₃ (reaction 6), but the presence of Mg and MgO controls its inhibiting effects. The oxidation of MgB₂ is initiated with the release of Mg vapor, which then oxidizes into MgO and is deposited on the surface, and the remaining B is oxidized to B₂O₃ (reaction 7). These reactions are exothermic (Table 3), and all contribute to the overall heat release. Thus, Mg/B solid solutions (36 kJ/g) have 24% and 38% higher heat release than B (29 kJ/g) and Mg/B mechanical mixtures (26 kJ/g), respectively. The broader exothermic peak during the oxidation of Mg/B solid solutions is due to the synergy of oxidation and redox reactions (reactions 5, 6, and 7) discussed above.

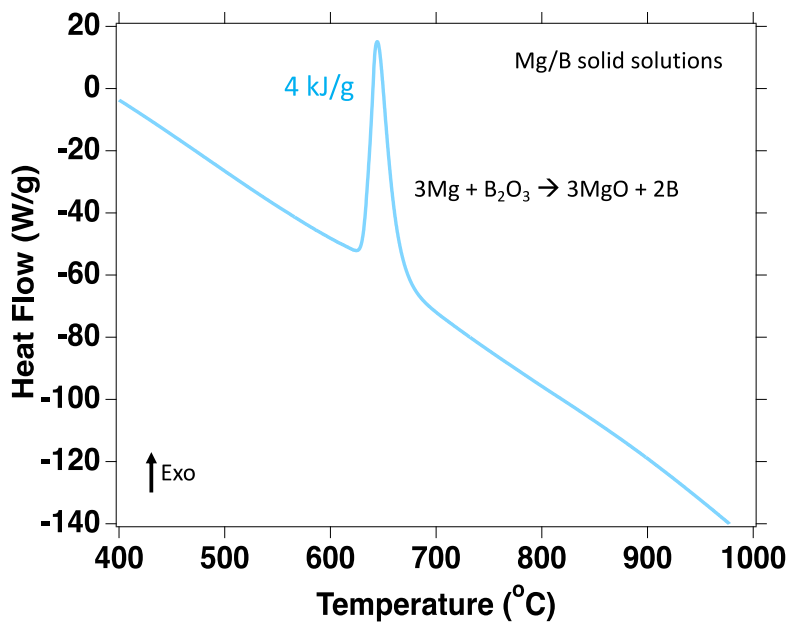


Figure 7. DSC analysis in an inert (Ar) atmosphere. The exotherm for the Mg/B solid solutions in Ar is attributed to a redox reaction between Mg and B₂O₃.

Table 3. Possible chemical reactions during the oxidation of Mg/B solid solutions.

Reaction number	Chemical Reaction	Oxidation Enthalpy (ΔH°) at 25°C (kJ/g)
5	$2\text{Mg}(\text{g}) + \text{O}_2(\text{g}) \rightarrow 2\text{MgO}(\text{s})$	-25
6	$2\text{B}(\text{s}) + 3/2\text{O}_2(\text{g}) \rightarrow \text{B}_2\text{O}_3(\text{l})$	-58
7	$\text{MgB}_2(\text{s}) + 2\text{O}_2(\text{g}) \rightarrow \text{MgO}(\text{s}) + \text{B}_2\text{O}_3(\text{l})$	-40

The presence of Mg, MgO, and MgB₂ in the near-surface region promotes the oxidation of B and minimizes the sintering effect of B₂O₃ by elevating the temperature at the interface and delaying the formation of B₂O₃ during thermal oxidation. The smaller particle size of the starting materials (B, Mg) causes maximum interfacial contact during the SHS reaction forming Mg/B solid solutions (average particle size: 550 nm) that leads to their near-complete oxidation and higher heat release compared to micron-sized materials [6, 21, 38, 41]. We can extract 90% of the energy stored in the Mg/B system during oxidation up to 1000°C (Table 1). Mg/B solid solutions are preferred over Mg/B mechanical mixtures because of the enhanced heat release upon oxidation (38% higher) and longer shelf life due to the presence of a passivation shell on the surface. Solid solutions of Mg/B should demonstrate better performance when dispersed in liquid fuels compared to Mg/B mechanical mixtures due to the possibility that Mg and B will not remain in proximity of each other when dispersed, which can reduce the benefits of physically mixing Mg with B [36, 37, 39].

5. CONCLUSIONS

We synthesized and characterized energetic Mg/B solid solutions with an average particle size of 550 nm by a self-propagating high-temperature solid-state synthesis (SHS) reaction between submicron-sized particles of B and Mg. The synthesis conditions were designed to maintain

maximum contact between Mg and B particles and minimize sintering of the product. Liquid Mg comes into direct contact with the surface of B particles to form a commensurate MgO/MgB₂ layer. Due to the presence of the Mg/B interface, the exothermic heat release due to the combustion of B increased by 24% compared to untreated B (for a temperature up to 1000°C) as shown by DSC analysis. TGA clearly indicates the promotional effect of Mg on the oxidation of B. High thermal stability and identical heat release after six months of storage suggest effective passivation and increased shelf life of the solid solutions. XPS, XRD, and STEM-EDS results show the presence of Mg, MgB₂, and MgO in the synthesized particles. The synergistic effect of oxidation of Mg, B, and MgB₂ coupled with the redox reaction between Mg and B₂O₃ lead to the increased heat release from Mg/B solid solutions, which is 90% of the theoretical energy density of Mg/B systems. These results can lead to the development of energetic materials with enhanced reactivity and heat release using a dry powder-based technique. The method developed in this study can be implemented in the design of energetic materials for the enhanced combustion of solid and liquid fuels.

SUPPORTING INFORMATION

The Supporting Information is available free of charge at

Comparison between heat release of the mechanical mixtures of Mg/B and Mg/B solid solutions during thermal oxidation; Thermodynamic analysis of potential reactions during the synthesis of Mg/B solid solutions; HAADF-STEM demonstrates a broad particle size distribution in the Mg/B solid solutions; Comparison of exothermic oxidation in Mg/B solid solutions: between the freshly synthesized sample and sample stored for 6 months

AUTHOR INFORMATION

*Corresponding author

Email address: txm11@psu.edu; Tel.: +1-814-863-2002

ORCID

Prawal Agarwal: 0000-0002-8795-6077
Devon Jensen: 0000-0001-5890-3972
Chien-Hua Chen: 0000-0002-2936-9528
Robert Rioux: 0000-0002-6019-0032
Themis Matsoukas: 0000-0002-0097-2673

ACKNOWLEDGMENTS

This work was supported by DOD SBIR under contract #N6893619C0015. We gratefully acknowledge support from the United States Navy (Dr. Ben Harvey). We are also thankful to the Material Characterization Lab (MCL) at Pennsylvania State University.

FINANCIAL INTEREST STATEMENTS

The authors declare no conflict of interest.

REFERENCES

1. Hui, X., Kumar, K., Sung, C.J., Edwards, T., Gardner, D.” Experimental studies on the combustion characteristics of alternative jet fuels”, *Fuel* 98,176–182, 2012
2. Chung, H.S., Chen, C.S.H., Kremer, R.A., Boulton, J.R., Burdette, G.W. Recent developments in high-energy density liquid hydrocarbon fuels, *Energy & Fuels* 13,641–649, 1999
3. Dreizin, E.L., “Metal-based reactive nanomaterials”, *Progress in Energy and Combustion Science*, 35(2), pp. 141–167, 2009
4. Yetter R.A., Risha G.A., Son, S.F., “Metal particle Combustion and Nanotechnology”, *Proceedings of Combustion Institute*, 32, pp. 1819-1838, 2009
5. Ojha, P. K.; Maji, R.; Karmakar, S. Effect of crystallinity on droplet regression and disruptive burning characteristics of nanofuel droplets containing amorphous and crystalline boron nanoparticles, *Combustion and Flame*, Volume 188, 2018, Pages 412-427
6. Karmakar, Srinibas. Energetic Nanoparticles as Fuel Additives for Enhanced Performance in Propulsion Systems (2012). LSU Doctoral Dissertations. 3614.

7. Ojha, P.K.; Karmakar, S. Boron for liquid fuel Engines-A review on synthesis, dispersion stability in liquid fuel, and combustion aspects. *Progress in Aerospace Sciences*, 100, 18-45, 2018
8. Jiang, Y.; Yilmaz, N. E. D.; Barker, K. P.; Baek, J.; Xia, Y.; Zheng, X. Enhancing Mechanical and Combustion Performance of Boron/Polymer Composites via Boron Particle Functionalization. *ACS Appl. Mater. Interfaces*, 13, 24, 28908-28915, 2021
9. Hosmane, N. S. *Boron Science New Technologies and Applications*, 1st ed.; Taylor & Francis Group: Boca Raton, FL, 2012
10. Hosmane, N. S.; Eagling, R. *Handbook of Boron Science with Applications in Organometallics, Catalysis, Materials and Medicine*; World Scientific: Singapore, 2019
11. Zhu, Y.; Prommana, P.; Hosmane, N.S.; Coghi, P.; Uthaipibull, C.; Zhang, Y. Functionalized Boron Nanoparticles as Potential Promising Antimalarial Agents, *ACS Omega* 2022 7 (7), 5864-5869
12. Zhou, X.; Torabi, M.; Lu, J.; Shen, R.; Zhang, K. Nanostructured Energetic Composites: Synthesis, Ignition/Combustion Modeling, and Applications. *ACS Appl. Mater. Interfaces* 2014, 6, 3058–3074.
13. Malchi, J. Y.; Foley, T. J.; Yetter, R. A. Electrostatically Self-Assembled Intermetallics Reactive Microspheres. *ACS Appl. Mater. Interfaces* 2009, 1, 2420–2423.
14. Zhou, X.; Xu, D.; Zhang, Q.; Lu, J.; Zhang, K. Facile Green in situ Synthesis of Mg/CuO Core-shell Nanoenergetic Arrays with Superior Heat Release Property and Long-Term Storage Stability. *ACS Appl. Mater. Interfaces* 2013, 5, 7641–7646.
15. Shahravan, A.; Desai, T.; Matsoukas, T. Passivation of aluminum nanoparticles by plasma-enhanced chemical vapor deposition for energetic nanomaterials, *ACS Applied Materials & Interfaces*, vol. 6, no. 10, pp. 7942–7947 (2014).
16. Bellott, B.J.; Noh, W.; Nuzzo, R.G.; Girolami, G.S. Nanoenergetic materials: boron nanoparticles from the pyrolysis of decaborane and their functionalization. *Chem Commun* 22:3214–3215 (2009).
17. Pickering AL, Mitterbauer C, Browning ND, Kauzlarich SM, Power PP “Room temperature synthesis of surface functionalised boron nanoparticles”. *Chem Commun* 6:580–582 (2007).
18. Ojha, P. K.; Karmakar, S. Effect of Silane Capping on the Dispersion and Combustion Characteristics of Sub-micrometer Boron Particles Loaded in Jet A-1, *Energy & Fuels* 2018 32 (10), 11010-11022
19. Agarwal, Prawal P. K.; Jensen, Devon; Chen, Chien-Hua; Rioux, Robert M.; Matsoukas, Themis. Surface-Functionalized Boron Nanoparticles with Reduced Oxide Content by

- Nonthermal Plasma Processing for Nanoenergetic Applications, ACS Appl. Mater. Interfaces 2021, 13, 5, 6844–6853.
20. Mota JM, Abenojar J, Martinez MA, Velasco F, Criado AJ. Borides and vitreous compounds sintered as high-energy fuels. *J Solid State Chem.*, 177:619–27(2004).
 21. Guo, Y., Zhang W., Zhou, X. Magnesium boride sintered as high-energy fuel. *J Therm Anal Calorim* 113, 787-791, 2013
 22. Schoenitz M, Dreizin EL, Shtessel E. Constant volume explosions of aerosols of metallic mechanical alloys and powder blends. *J Propuls Power*, 19:405–12 (2003).
 23. Ojha, P. K.; Karmakar, S. Combustion Characteristics of Jet A-1 Droplet Loaded with Aluminum/Magnesium-decorated Boron Particles, *International Journal of Energetic Materials and Chemical Propulsion*, 19(3):253–274 (2020)
 24. Liu TK, Luh SP, Perng HC. Effect of boron particles surface coating on combustion of solid propellants for ducted rockets. *Propellants, Explos, Pyrotech.* 1991;16:156–66.
 25. Yeh CL. Ignition and combustion of boron particles. The Pennsylvania State University, Ph.D Thesis; 1995.
 26. Hashim, S.A.; Karmakar, S.; Roy, A. Effects of Ti and Mg particles on combustion characteristics of boron–HTPB-based solid fuels for hybrid gas generator in ducted rocket applications, *Acta Astronautica*, Volume 160, 2019, Pages 125-137
 27. Liu, X.; Chinter singh, K.L. ; Schoenitz, M.; Dreizin, E. L. Reactive composite boron–magnesium powders prepared by mechanical milling, *J. Propul. Power* 34 (3) (2017) 787–794.
 28. Liang, D.; Xiao, R.; Liu, J.; Wang, Y.; Ignition and heterogeneous combustion of aluminum boride and boron–aluminum blend, *Aerospace Science and Technology*, 84 (2019), 1081-1091
 29. Il'n, A. P.; Yablunovskii, G. V.; Gromov, A. A.; Popenko, E. M.; Bychin N. V. Combustion of mixtures of ultrafine powders of aluminum and boron in air, *Combustion, Explosion, and Shock Waves* Vol 35, No. 6 (1999), 656-659
 30. Kim, D.W.; Kim, K.T.; Kwon, G.H.; Song, k.; Son, I. Self-Propagating Heat Synthetic Reactivity of Fine Aluminum Particles via Spontaneously Coated Nickel Layer. *Nature Sci Rep* 9, 1033 (2019).
 31. Kerri-Lee Chintersingh, Mirko Schoenitz & Edward L. Dreizin Effect of Purity, Surface Modification and Iron Coating on Ignition and Combustion of Boron in Air, *Combustion Science and Technology* 193:9, 1567-1586 (2019)
 32. Prachukho, V.P.; Ozerov, E.S.; Yurinov, A.A. Burning of magnesium particles in water vapor, *Combust. Explos. Shock Waves* 7 (2) (1971) 195–198.

33. Li, C.; Hu, C.; Zhu, X.; Hu, J.; Li, Y.; Hu, X. Experimental study on the thrust modulation performance of powdered magnesium and CO₂, bipropellant engine, *Acta Astronaut.* 147 (2018) 403–411.
34. Law, C.K.; Williams, F.A. Combustion of magnesium particles in oxygen-inert atmospheres [J], *Combust. Flame* 22 (3) (1974) 383–405.
35. Sandall, E.T.; Kalman, J.; Quigley, J.N.; Munro, S.; Hedman, T.D. A study of solid ramjet fuel containing boron–magnesium mixtures, *Propul. Power Res.* 6 (4) (2017) 243–252.
36. L. Liu, P. Liu, G. He, Ignition and combustion characteristics of compound of magnesium and boron, *J. Therm. Anal. Calorim.* 121 (3) (2015) 1205–1212.
37. Jung, W.; Yun, Y.; Kim, K.S.; Park, J.; Kwon, S. Performance Evaluation of Ramjet Fuel Grains with Boron and Magnesium Additives [C]//2018 Joint Propulsion Conference, 2018, p. 4873.
38. Sun, Y.; Ren, H.; Du, F.; Yan, S.; Jiao, Q. Preparation and characterization of sintered B/MgB₂ as heat release material, *Journal of Alloys and Compounds*, Volume 759, 2018, 100-107
39. Liu, J.; Xi, J.; Yang, W.; Hu, Y.; Zhang, Y.; Wang, Y.; Zhou, J. Effect of magnesium on the burning characteristics of boron particles, *Acta Astronaut.* 96 (2014) 89–96.
40. Liu, Z.; Schlom, D. G.; Li, Q.; Xi, X. X. Thermodynamics of the Mg–B system: Implications for the deposition of MgB₂ thin films, *Appl. Phys. Lett.* 78, 3678 (2001)
41. Liang, D.; Xiao, R.; Li, H.; Liu, J. Heterogeneous decomposition and oxidation during combustion of magnesium diboride particles”, *Acta Astronautica* 153, 159–165 (2018)
42. Seah, M.P. Summary of ISO/TC 201 Standard: VII ISO 15472:2001 — surface chemical analysis — x-ray photoelectron spectrometers — calibration of energy scales. *Surf. Interface Analysis* 31 721-723 (2001)
43. Yin, Y.; Rioux, R.M.; Erdonmez, C.K.; Hughes, S.; Somorjai, G.A., Alivisatos, A.P. Formation of hollow nanocrystals through the nanoscale Kirkendall effect, *Science*, 304 (5671) (2004), p. 711
44. Bello, M.N.; Pantoya, M.L.; Kappagantula, K.; Wang, W.S.; Vanapalli, S.A.; Irvin, D.J.; Wood, L.M. Reaction Dynamics of Rocket Propellant with Magnesium Oxide Nanoparticles *Energy & Fuels* **2015** 29 (9), 6111-6117
45. Chintersingh, Kerri-Lee; Schoenitz, M.; Dreizin, E.L. Oxidation Kinetics and Combustion of Boron Particles with Modified Surface. *Combustion and Flame*, Volume 173, 2016, Pages 288-295.